PHYSICS

Mid-infrared polarization-controlled broadband achromatic metadevice

Kai Ou[1,2,3,4]*, Feilong Yu[1,2,3,4]*, Guanhai Li[1,2,3,4†], Wenjuan Wang[1,4], Andrey E. Miroshnichenko[5†], Lujun Huang[5], Peng Wang[1,4], Tianxin Li[1,4], Zhifeng Li[1,4], Xiaoshuang Chen[1,2,3,4†], Wei Lu[1,2,3,4]

Metasurfaces provide a compact, flexible, and efficient platform to manipulate the electromagnetic waves. However, chromatic aberration imposes severe restrictions on their applications in broadband polarization control. Here, we propose a broadband achromatic methodology to implement polarization-controlled multifunctional metadevices in mid-wavelength infrared with birefringent meta-atoms. We demonstrate the generation of polarization-controlled and achromatically on-axis focused optical vortex beams with diffraction-limited focal spots and switchable topological charge ($L^{\parallel} = 0$ and $L^{\perp} = 2$). Besides, we further implement broadband achromatic polarization beamsplitter with high polarization isolation (extinction ratio up to 21). The adoption of all-silicon configuration not only facilitates the integration with CMOS technology but also endows the polarization multiplexing meta-atoms with broad phase dispersion coverage, ensuring the large size and high performance of the metadevices. Compared with the state-of-the-art chromatic aberration–restricted polarization-controlled metadevices, our work represents a substantial advance and a step toward practical applications.

INTRODUCTION

Refractive optics and conventional diffractive optics (such as Fresnel zone plates) play an indispensable role in modern optics and have tremendous applications in our daily life. Metasurfaces provide a fundamentally new methodology for effectively manipulating the light field, benefitting from the custom-tailorable and planar meta-atom engineering. They provide highly efficient and accurate control of amplitude, phase, wavelength, polarization, and other basic parameters in subwavelength spatial resolutions (*1*–*6*). It has brought unprecedented freedom over their traditional bulky and heavy counterparts in developing the ultracompact and integrated photonic systems, such as nanoscale light source (*7*–*10*), meta-holograms (*11*–*13*), and nonlinear optics (*14*, *15*).

Recent progress in the photonic system poses an urgent demand on miniaturized and integrated optical elements. This pushes the metasurfaces toward the direction of simultaneous manipulation of multidimensional light field. Various metadevices are thus proposed via encoding the amplitude, phase, wavelength, or polarization information with desired functionalities onto a single metasurface (*16*–*22*). The on-chip polarimetry has been demonstrated with comparable performance to the commercial ellipsometry in characterizing the chiral samples in visible (*23*). Among them, the focusing devices with polarization control have attracted great attention because of the low cross-talk and high operating efficiency (*24*–*28*). Several works on the dispersion control have also been reported to resolve the problem on the multiple discrete wavelengths or narrowband achromatism (*29*–*31*).

It is always desired to have an achromatic metasurface with powerful functionalities and even more compact size. Several pioneering works on broadband achromatic metadevices (BAMs) have been proposed and summarized in visible and near infrared (*32*–*37*), and the devices operate with excellent performance in terms of nearly diffraction-limited focusing and full-color imaging. In (*34*), GaN-based achromatic metalens demonstrates a high-average efficiency up to 40% in visible, which is a substantial advance of the broadband achromatic metalens. Polarization-dependent functional metadevices based on the utilization of geometric phase structures and polarization-insensitive single-function metadevice with symmetric structures are also well demonstrated. Besides, three-dimensional (3D)–printed multicomponent micro-optics devices have been reported, which show outstanding performance on correcting aberration, realizing large field of views and compactly integrating with current complementary metal oxide semiconductor (CMOS) cameras (*38*, *39*). Up to now, there is no work reporting the broadband achromatic multifunctional metadevices (BAMMs) with polarization control. In addition, the phase dispersion control is generally realized through refractive index contrast platform, which deposits high-index materials on the low-index substrates. Moreover, very few metasurfaces have been reported in the mid-wavelength infrared (MWIR), which has many practical applications, such as molecular fingerprint detection, low-light-level night version, and free-space communications. Compared with the visible and near-infrared counterparts, the relative immaturity of conventional MWIR optics offers a potential opportunity to develop the compact, highly efficient, and compatible optical multidimensional metadevices in this regime.

The phase dispersion is fundamentally bounded by the meta-atom's height divided by the group index. As to the material's option to realize achromatism, both high–refractive index and lossless materials within the bandwidth of interest should be fulfilled. In this work, we propose a generally broadband achromatic approach to simultaneously engineer the phase dispersion and the polarization based on all-silicon birefringent metasurface. This all-Si platform not only makes us free from the additional material's deposition but also provides us a straightforward way to achieve on-demand phase

dispersion control range. Different from the 3D-printed achromatic devices based on the aspheric surface design and multicomponent materials in (39), the metadevice design featuring planar configuration and subwavelength meta-atom scale in our work is demonstrated as a generally achromatic approach to simultaneously and elaborately manipulate the phase dispersion and the polarization based on all-silicon birefringent metasurface. For the proof of concept, we design and fabricate two polarization-controlled BAMMs within the continuous bandwidth from 3.5 to 5 μm: the on-axis broadband achromatic focusing optical vortex generator (BAFOV) and the off-axis bifocal broadband achromatic focusing splitter (BAFS). First, the BAFOV generator is conducted to convert the broadband incident beam into the focused optical vortex (OV) beams with distinct and polarization-controlled topological charge number ($L^{\parallel}$=0 and $L^{\perp}$=2) on the focal plane. Next, we demonstrate the BAFS with diffraction-limited broadband achromatic focusing behavior and show that the positions of the focal spots can be alternatively switched through changing the incident polarization state. High polarization isolation is also demonstrated. The experimental and simulated results robustly confirmed our approach.
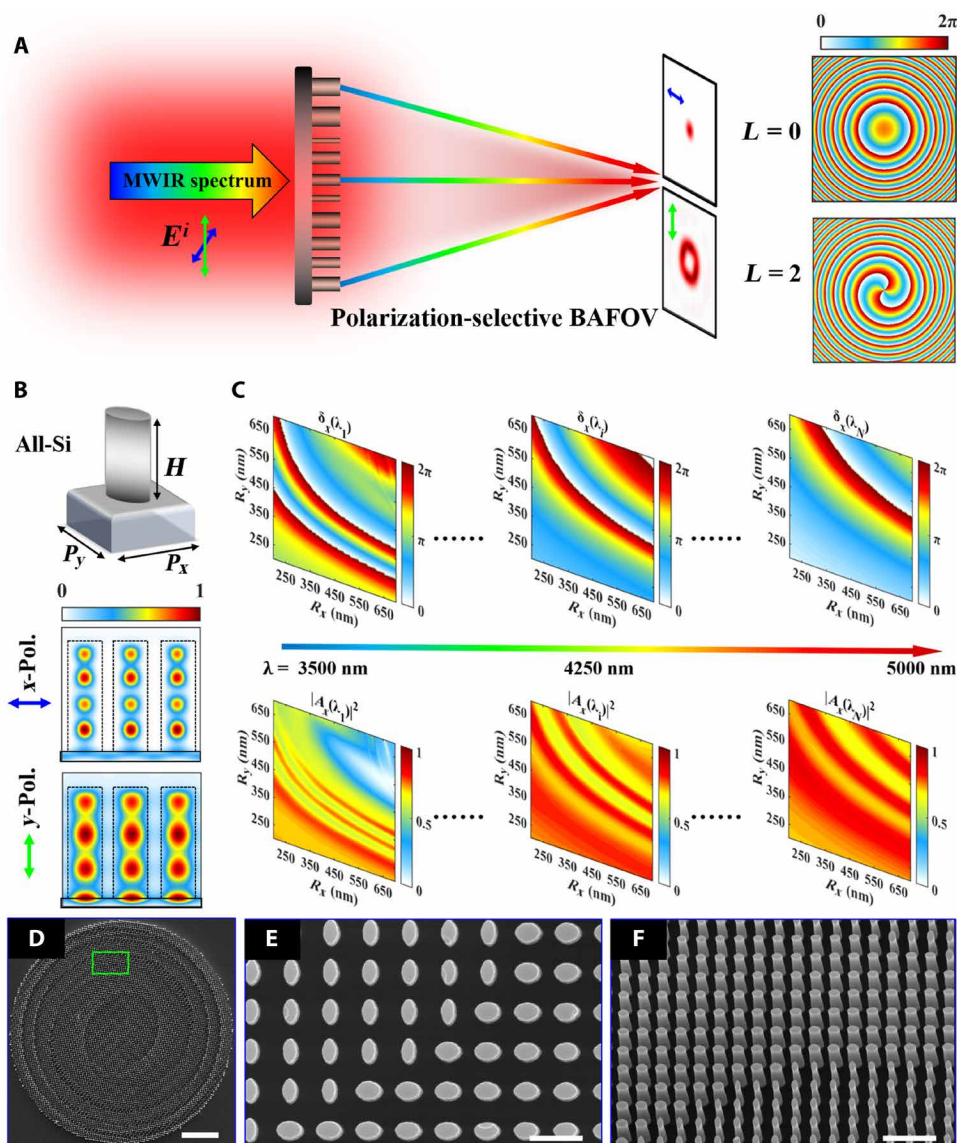

Fig. 1. Schematic of BAFOV generator, the birefringent meta-atom library, and SEM images of the samples. (**A**) Schematic illustration of the BAFOV generation with polarization-dependent functions. The MWIR beam is normally incident on the metasurface from the substrate. The transmitted light is achromatically focused at prescribed focal planes with different topological charge numbers according to the incident polarization state. (Top) The phase profile of l = 0 for x-polarization and (bottom) l = 2 for y-polarization. Blue and green double-headed arrows shown in (A) represent the x- and y-polarization, respectively. (**B**) The birefringent meta-atoms are made of monocrystalline Si (top). The thickness of the pattern layer of the all-Si metasurface is H = 4500 nm. Bottom: The polarization-dependent magnetic energy density profile along the x-z cross section in the periodic array with D_x = 1160 nm and D_y = 700 nm. Black dotted lines depict the boundaries of the nanoposts. (**C**) The meta-atom library is composed of the transmittance and phase spectra based on the meta-atom engineering through sweeping wavelength from 3.5 to 5 μm. (**D** to **F**) SEM images of the fabricated polarization-controlled BAFOV. (D) Overall SEM image of the metadevice. Scale bars, 27 μm. Top view [scale bar, 2 μm (E)] and oblique view [scale bar, 4 μm] of part of the sample [marking with the green frame shown in (D)].

RESULTS
Principle of polarization-controlled BAMMs
To establish the relationship between the functions of polarization control and birefringent meta-atoms, we consider the polarization-dependent phasors $A_m^{\parallel}(\lambda)\,e^{j\delta_m^{\parallel}(\lambda)}$ and $A_m^{\perp}(\lambda)\,e^{j\delta_m^{\perp}(\lambda)}$ imposed on the incident light by the birefringent meta-atom on each pixel of the metadevices. The response can be modulated by adjusting D_x and D_y—the major and the short axis of nanopillars. To introduce the focused chromatic aberration correction effect, the polarization-dependent phase profiles of the metadevices should be functions of pixel coordinate and wavelength

$$\varphi^i(r,\lambda) = \frac{2\pi}{\lambda}\left(-\left(\sqrt{r^2 + (F_0^i)^2} - F_0^i\right) + x\sin(\Theta_0^i) + C_0^i\right) + L^i\theta, (i = \parallel,\perp) \quad (1)$$

where F_0^i, Θ_0^i, and L^i are the focal length, deflection angle, and topological charge number for different polarization states, respectively. $r = \sqrt{x^2 + y^2}$ and $\theta = \arctan\frac{y}{x}$ are the radial and azimuth coordinates, respectively. C_0^i is an arbitrary but polarization-dependent constant that determines the reference phase at each wavelength. A spatial Jones matrix can thus describe the overall function of the metadevice

$$J(r,\lambda) = \begin{bmatrix} A^{\parallel}\,e^{j\varphi^{\parallel}(r,\lambda)} & 0 \\ 0 & A^{\perp}\,e^{j\varphi^{\perp}(r,\lambda)} \end{bmatrix} \quad (2)$$

where $A^{\parallel}e^{j\varphi\parallel(r,\lambda)}$ and $A^{\perp}e^{j\varphi\perp(r,\lambda)}$ are the desired phasors for x-polarization (horizontal) and y-polarization (vertical) incidence, respectively.

Combining Eqs. 1 and 2, we can achieve the mapping between the polarization-dependent phasor $A_m^i(\lambda)\,e^{j\delta_m^i(\lambda)}$ imposed by the meta-atom and the desired phasor $A^ie^{j\varphi i(r,\lambda)}$ at each pixel. The optimal combination of $C_0^{\parallel}$ and $C_0^{\perp}$ can be chosen by minimizing the summation of phasor error $\text{Error}(r,C_0^{\parallel},C_0^{\perp}) = \Sigma_i^{\parallel,\perp}\Sigma_{k=1}^{N+1}\left|A^i\,e^{j\varphi^i(r,C_0^i,\lambda_k)} - A_m^i(\lambda_k)\,e^{j\delta_m^i(\lambda_k)}\right|$ across the design wavelength and pixel coordinate. In this work, we set $A^i = 0.88$ according to the mean transmittance of the meta-atoms (as shown in Fig. 1C). Last, the mapping between the desired optical response at each pixel and the size of the birefringent meta-atoms is built. The double-polished monocrystalline silicon wafer is adopted to manufacture meta-atoms from one side. The thickness of the wafer is 500 μm. The refractive index of silicon is derived from (40). As the start of the design for our BAMMs, we performed full-wave simulations for extracting the polarization-dependent transmittance $[(A_m^i(\lambda))^2]$ and phase spectrum $[\delta_m^i(\lambda)]$ functioning as the size of the meta-atom (the simulated details are shown in Materials and Methods).
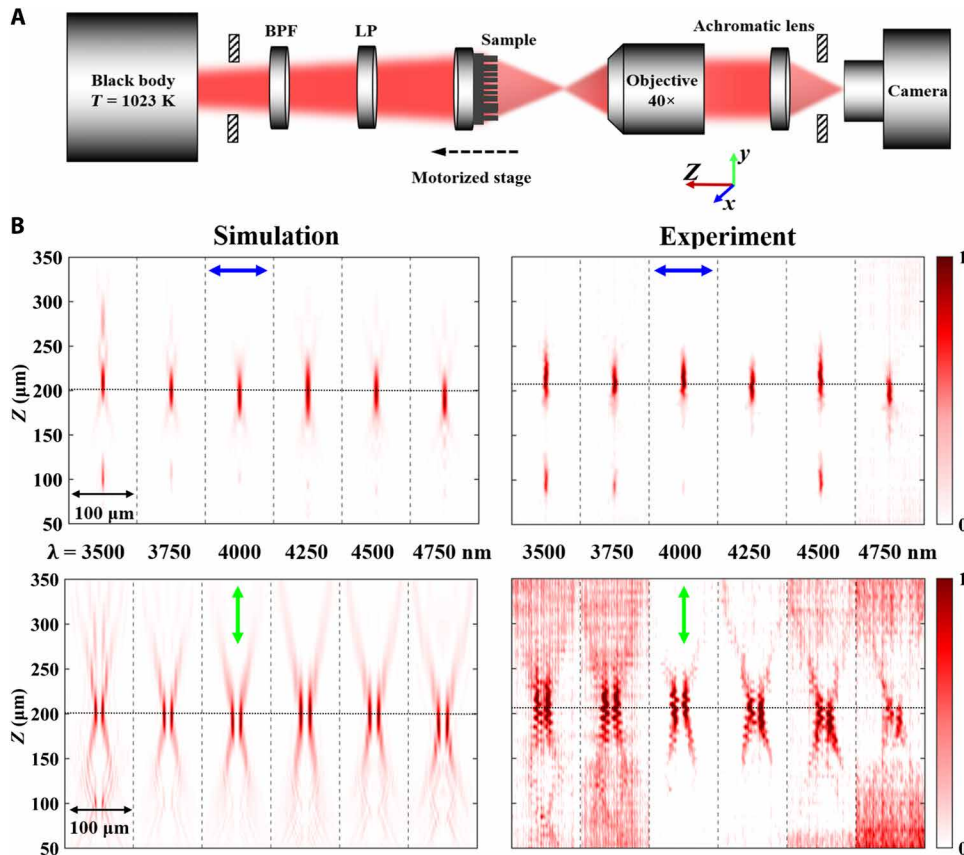

Fig. 2. Experiment setup and characterization of BAFOV. (**A**) Characterizing system for the measurement of fabricated metadevices. (**B**) Measured (right) and simulated (left) intensity profiles along the axial plane within the overall designed waveband from 3.5 to 5 μm for x-polarization (top) and y-polarization (bottom) polarization, respectively. More simulations (including the simulated result at the wavelength of 5 μm) can be found in fig. S4. The black dashed lines indicate the positions of the mean focal lengths for all the sampled wavelengths. LP, linear polarizer; BPF, bandpass filter.

Birefringent meta-atom design and characterization of the BAFOV metadevice

Figure 1A illustrates the generation of BAFOV, which can achromatically focus the broadband incidence at the designed focal plane. The focused OV beams can carry different topological charge numbers, depending on the polarization of the incident light. As shown in Fig. 1B, our metadevices are composed of elliptical silicon nanoposts arranged in a square lattice with period $P_x = P_y = 1650$ nm. Such elliptical nanoposts can be considered as a truncated waveguide with birefringent effect originating from the different waveguide modes polarized along the two orthogonal ellipse axes. The field distributions (bottom) in Fig. 1B reveal the polarization-dependent waveguide effect ($D_x = 1160$ nm and $D_y = 700$ nm). The strong optical energy confinement in the nanopillar indicates that the polarization and wavefront manipulation with the meta-atoms are a localized effect. Figure 1C shows the library (phase and transmittance spectra) as a function of D_x and D_y, which both range from 400 to 1400 nm. Because of the symmetry, the library for y-polarization incidence and that for x-polarization are mirror symmetry with respect to the diagonal line that corresponds to $R_x = R_y$ (semi-axis length of the elliptical nanopillar). The spectra exhibit a polarization-dependent optical response but with low cross-talk, which means that we can independently and efficiently tailor the phase along the different axis at subwavelength scale.

The adoption of birefringent meta-atoms allows us to independently and effectively manipulate the phase and dispersion for the orthogonal linear polarizations at subwavelength scale over the broad bandwidth. The chromatic dispersion mainly arises from the resonant phase dispersion of the building meta-atoms and the intrinsic dispersion of the materials that are used to construct the meta-atoms. The polarization-controlled BAMs in our manuscript are realized through elaborately controlling the resonant phase dispersion and compensating the intrinsic phase dispersion with our all-Si birefringent meta-atom design. The broadband functionality is not due to the natural response of the materials in MWIR. The comparison between the polarization-controlled metadevice design with and without the dispersion control is shown in figs. S1 and S2 from section S1. On the basis of the proposed strategy, we designed and experimentally fabricated the BAFOV metadevice with a diameter of 200 μm ($\Theta_0^{\parallel,\perp} = 0$, $L^{\parallel} = 0$, $F_0^{\parallel} = 200$ μm, and $L^{\perp} = 2$, $F_0^{\perp} = 200$ μm). The scanning electron microscopy (SEM) images of the sample are shown in Fig. 1 (D and F) (see Materials and Methods for fabrication details). Figure 2A shows the experimental setup for characterization of our metadevices. Here, the blackbody at 1023 K behaves as a broadband infrared source. Six bandpass filters (BPF) (Thorlabs, FB-3500-500nm, FB-3750-500nm, FB-4000-500nm, FB-4250-500nm, FB-4500-500nm, and FB-4750-500nm) are adopted in the measurement at the sampled wavelengths. The switchable polarization behavior of the BAFOV generator can be confirmed by rotating the linear polarizer (LP) (Thorlabs, WP25LM-IRA) (see movies S1 to S3 for beam conversion details). The imaging equipment consisting of a 40× reflective microscope objective (Thorlabs, LMM-40X-P01), an achromatic
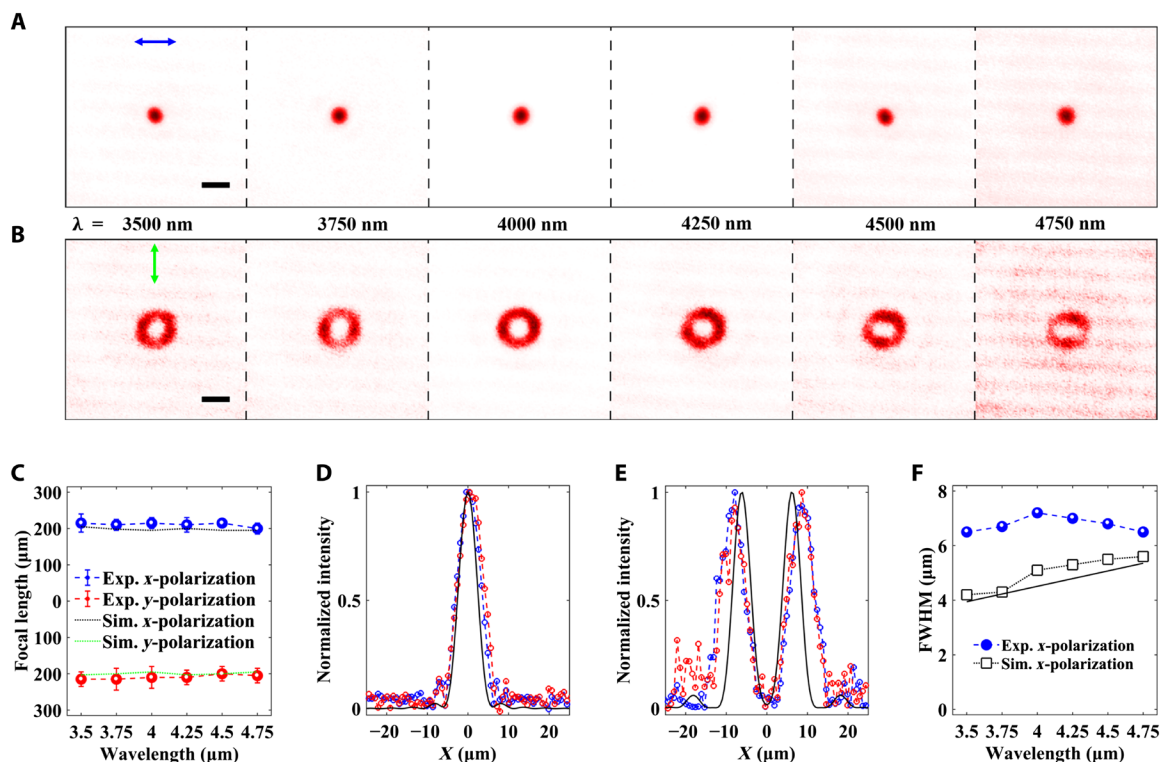

Fig. 3. Performance of the BAFOV generator. (**A** and **B**) Measured transverse intensity distributions along the black dotted line shown in Fig. 2B for each sampled wavelength. (A) is for x-polarization and (B) is for y-polarization. Scale bars, 15 μm. (**C**) Simulated and measured focal lengths as a function of wavelength. The error bars show the distance variations from the focal plane where the intensity of the focal spot remains the maximum value in the measurement. (**D** and **E**) Normalized horizontal- (blue dashed line) and vertical (red dashed line) cut intensity profiles of the focal spots shown in (A) and (B) at λ = 4000 nm, respectively. The content in the main text is also modified below. The black solid lines represent the corresponding simulated results. (**F**) Full width at half maximums (FWHMs) of the focal spots shown in (A) versus the sampled wavelengths. The solid line represents the corresponding theoretical diffraction limits. Exp., experiment. Sim., simulation.

doublet infrared lenses (Thorlabs, AC254-100-E), and an mercury cadmium telluride (MCT) camera (Xenics Onca MWIR-640) was used to capture the intensity images and evaluate the focusing performance of the metadevices. The samples were placed at a distance of 25 cm from the blackbody (with an aperture diameter of 2 mm) to approximate collimated and normal incidence. The motorized stage assembly was moved along the longitudinal direction (z axis) in steps of 2.5 μm for the measurements, and the reference position (i.e., device plane, $Z = 0$) was set when the camera can clearly capture the image of the samples.

With this setup, we characterized the spatial intensity distributions of the modulated light field through measuring the intensities on the transverse planes along the z axis at predefined wavelengths. Because of the lack of MWIR high-power broadband lasers and high-sensitivity photon detectors, the measurement is more difficult and challenging than those in the shorter wavelength. The MWIR camera in our measurement is cooled to about 80 K, but the performance is even worse than those of some silicon-based cameras operating at room temperature. Figure 2B shows the simulated (left) and measured (right) intensity profiles along with longitudinal directions for the x-polarized (top) and y-polarized (bottom) incidence. It can be seen that solid-spot and hollow-shaped beams with centers on almost the same focal lengths are generated, respectively. To better illustrate the beams, Fig. 3 (A and B) shows the transverse intensity profiles along the dotted lines shown in Fig. 2B. The focal spots exhibit the polarization-dependent behavior (topological charge number depends on the incident polarization). The experimental results agree well with the simulations. This robustly confirms the achromatic focusing property and polarization-switchable behavior of the BAFOV generator (see simulated transverse intensity profiles and phase distribution profiles of the beams in fig. S5 of section S3).

As shown in Fig. 3C, the simulated and measured focal lengths show minor discrepancy (maximum 5% derivation relative to the mean focal length) for all the sampled wavelengths. The results further prove that the BAFOV metadevice effectively generates achromatic focus-ing beams with different topological charge numbers according to the incident polarization. Figure 3 (D and E) shows the horizontal and vertical cuts intensity profiles across the focal spots. The measured results are very close to the simulations. Figure 3F summarizes the corresponding full width at half maximum (FWHM) spectrum, together with the simulations and theoretical limits for comparison. The results experimentally demonstrate the nearly diffraction-limited focusing and polarization-dependent behavior. The BAMM based on the all-Si design strategy paves the promising way to integrate with the existing CMOS systems.

Design and characterization of the BAFS metadevice

To demonstrate the versatility of our design strategy, we fabricated a broadband achromatic polarization beamsplitter through encoding the off-axis phase term into Eq. 2 (setting $L^{\parallel,\perp} = 0$, $\Theta_0^{\parallel} = -5.5°$, $F_0^{\parallel} = 200$ μm, and $\Theta_0^{\perp} = 5.5°$, $F_0^{\perp} = 200$ μm; see SEM images of the sample in fig. S1 of section S3). The splitter can achromatically focus the incidence at two off-axis spots on the same focal plane according to the incident polarization. Different from the polarimetry that uses the intrinsic dispersion of the chromatic gradient metasurface reported in (23), the multifunctional metadevices in our work are designed to simultaneously engineer the phase dispersion and the polarization with all-silicon birefringent meta-atoms. Compared with the conventional bulk elements filtering the undesired polarization, different polarized photons in our work are not only sorted but also converged to the diffraction-limited focal spots via a polarization-controlled manner over a broad bandwidth from 3.5 to 5 μm. This approach here paves an innovative way to implement multidimensional control of the photons with ultracompact configuration and low cross-talk.

Using the same measurement setup, we characterized the focusing and polarization-controlled performance of the BAFS metadevice. Figure 4 (A and B) shows the intensity distributions of the transmitted field along x-z planes for x- and y-polarized incidence. As the theoretical design, the measured focal lengths of the spots keep almost the same
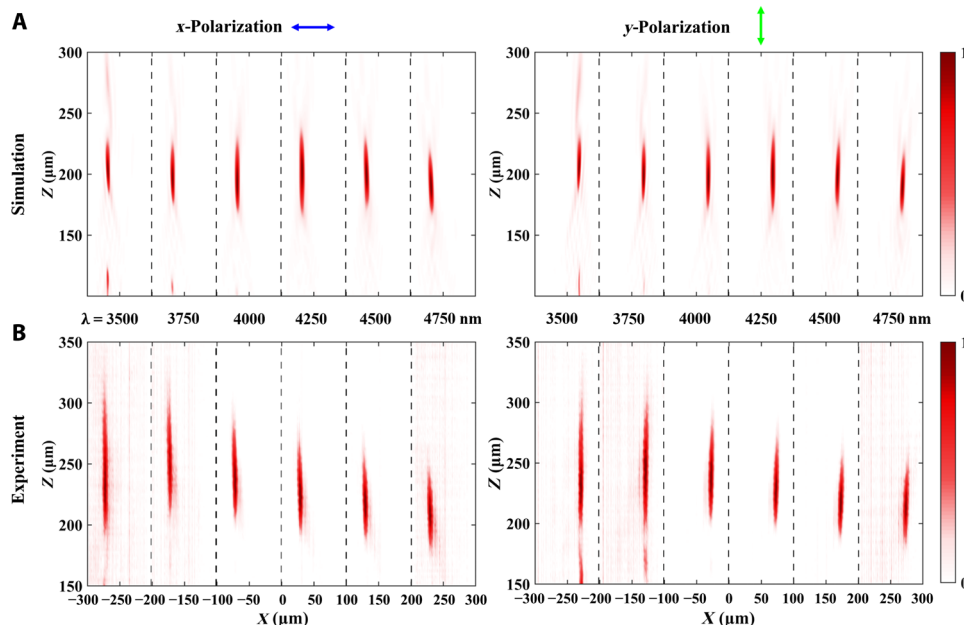

Fig. 4. Polarization-controlled behavior of the BAFS. (A) Simulated and **(B)** measured intensity profiles of the BAFS metadevice along with longitudinal directions at various incident wavelengths. The left panel is for x-polarized incidence, and the right panel is for y-polarization. More simulations can be found in fig. S6.

at each wavelength for different polarizations but at opposite directions ($\Theta_0^{\parallel,\perp} = \pm 5.5°$) due to the opposite off-axis phase shift imparted in Eq. 2. This phenomenon reveals the achromatic and polarization-controlled focusing behavior of the BAFS. Figure 5 (A and B) illustrates the transverse intensity profiles of focal spots in Fig. 4. Figure 5C shows the corresponding horizontal and vertical cut curves (normalized intensity distributions) of the focal spots shown in Fig. 5 (A and B). We also provide the measured results to demonstrate the dynamical conversion process through rotating the polarizer in movies S4 to S6. Also, more simulations are provided in figs. S6 and S7.

To further characterize the property of the BAFS metadevice, we summarize the focal length deviation, the horizontal shifts of the focal spot (ΔX), the polarization isolation, and the FWHMs of the focal spot in Fig. 5 (D to G). Figure 5D shows the extracted focal length as a function of the wavelength, with small derivation from 1 to 6.5% relative to the mean focal length. The horizontal shift ΔX of the simulations and measurements in Fig. 5E shows excellent agreement with the corresponding theoretical values ($\pm F \times \tan \Theta_0$). Furthermore, high polarization isolation (the extinction ratio up to 21) shown in Fig. 5F is achieved, which further reveals the excellent light con-

vergence and polarization-controlled capability of the BAFS. Here, we defined the polarization isolation as the ratio of the optical power passing through a circular aperture (with a diameter of the FWHM spanning the center of the polarization-dependent focal spot) to the power on a circular region with the same size located at the mirror symmetry position of the focus with respect to the y axis. The measured and simulated FWHMs that demonstrate the realization of the nearly diffraction-limited focusing property are shown in Fig. 5G. Despite the imperfect fabrication and measurement worsening the metadevices, the above figures of merit definitely confirm that the BAFS metadevice operates with high performance.

DISCUSSION
We have demonstrated the polarization-controlled BAMMs in the MWIR. The essential birefringent property of the meta-atom provides with a new degree of freedom to realize different functions according to the polarization states. We experimentally demonstrated two polarization-controlled metadevices: the achromatic focused vortex beam generator with different topological charge
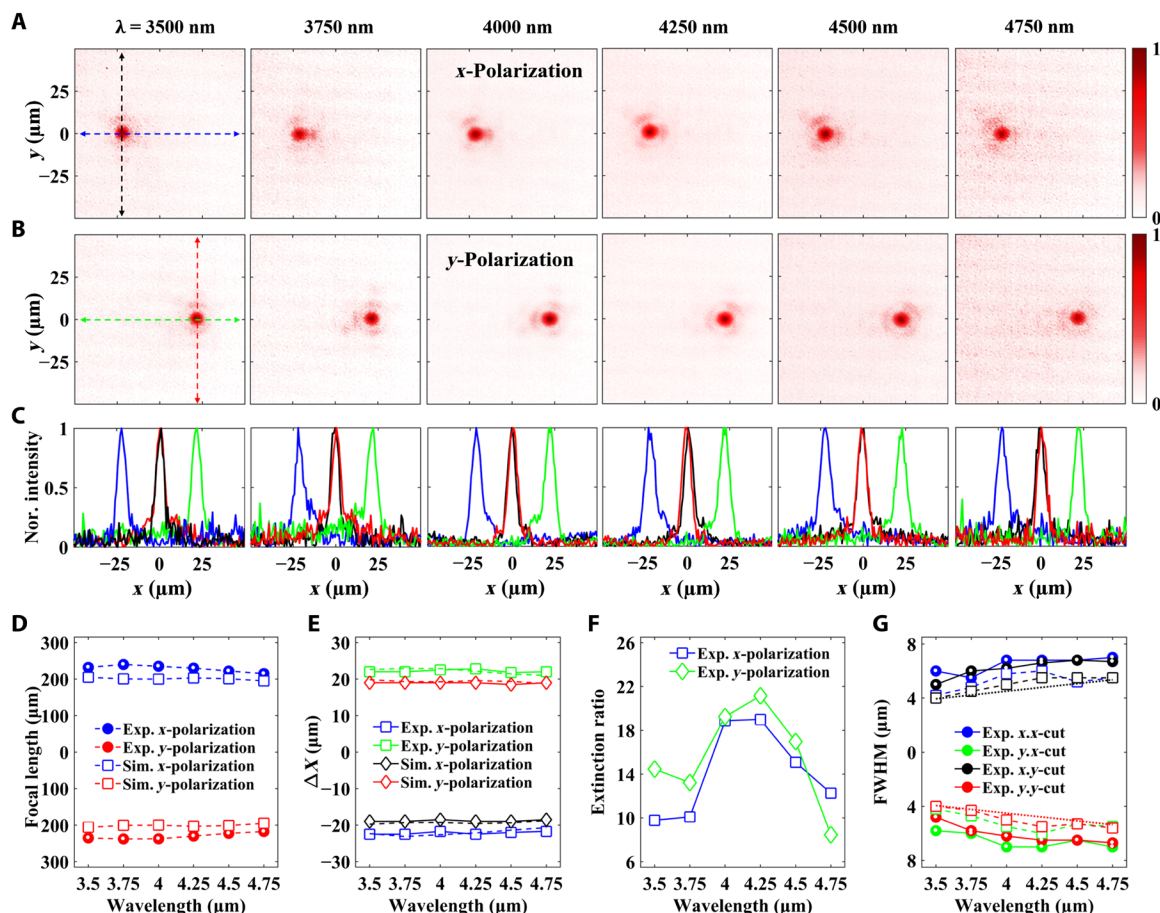

Fig. 5. Transverse intensity distributions and characterizations of the BAFS. (**A** and **B**) Measured focal plane intensity distributions are shown in Fig. 4B at each sampled wavelength for (A) x-polarization and (B) y-polarization. (**C**) Horizontal and vertical cuts [shown the dashed lines in (A) and (B)] across the measured focal spots for x-polarization (blue and black curves) and y-polarization (green and red curves) for the sampled wavelengths. Nor., normalized. (**D**) Measured and simulated focal lengths as a function of wavelength for both polarizations. (**E**) Measured and simulated horizontal shifts (ΔX) of the focal spots from the center for x- and y-polarized incidence at selected wavelengths. The dashed lines demonstrate the corresponding theoretical values ($\pm F \times \tan \Theta_0$) for comparisons. "$F$" is the corresponding focal length extracted in (D). (**F**) Measured extinction ratio at each sampled wavelength. (**G**) Extracted FWHMs of the focal spots along horizontal- and vertical-cut lines for x- and y-polarization in (C). Dashed curves represent the corresponding simulated results, and dotted straight lines represent the theoretical limits.

numbers and the focused beamsplitter with high polarization isolation. The use of all-silicon provides us some possible advantages in one or several merits in the following aspects: no additional film deposition, only one-step fabrication, easier integration with the current CMOS technology, and mature manufacturing. This polarization multiplex design represents a substantial advance in state of the art for achromatic focused metadevices, which have traditionally been limited to the polarization. The multifunctional BAMs may find various applications in optical information encryption, image switching, and encodings.

MATERIALS AND METHODS

Sample preparation

Chromium (Cr) is deposited 100 nm thick on one side of a cleaned double-sided polished monocrystalline silicon wafer with e-beam evaporation. The thickness of the wafer is 500 μm, which is confirmed by a step profiler (Bruker DektakXT). The negative photoresist (ma-N 2403) is coated at the speed of 3000 r/s for 30 s, baked on a hot plate at 90°. JEOL electron beam lithography (JBX-6300FS) is used to generate the patterns with a dose of 340 μC/cm^2 at a current of 500 pA with 100-kV accelerating voltage. The resist is then developed in 300-MIF solution for 30 s and thoroughly rinsed with deionized water for about 5 min. Inductively coupled plasma (Oxford ICP 180) in a mixture of Cl_2 [45 standard cubic centimeter per minute (sccm)] and O_2 (4 sccm) with an radio frequency (RF) power of 10 W is used to etch the chromium. Afterward, the pattern is transferred to silicon with protection of Cr hard mask. This silicon is etched in a mixture of SF_6 (50 sccm) and C_4F_8 (100 sccm) at 10°C with an RF power of 50 W by ICP (Oxford 380). The chromium is lastly removed using ICP 180.

Numerical simulations

All numerical simulations are conducted by using 3D finite-difference time-domain (FDTD) simulations. To obtain the database of the building blocks used in metadevice design, periodic boundary conditions are applied along the x and y axes and perfectly matched layers (PMLs) along the z axis (direction of light propagation). The periodic arrays are illuminated with x- and y-polarized plane waves within the wavelengths ranged from 3.5 to 5 μm, respectively. Subsequently, the transmission spectra ($A_m^{\parallel,\perp}(\lambda)$) and phase shift spectrum ($\delta_m^{\parallel,\perp}(\lambda)$) of the meta-atoms are extracted from the simulations for constructing the polarization-dependent library (see sections 2.1 and 2.2). The refractive index of monocrystalline silicon is obtained from (40). In the design process of polarization-controlled BAMMs, first, the optimal $C_0^{\parallel,\perp}$ is determined by minimizing the summation of the figure of merit [minimum of phasor error summation $Error(r, C_0^\parallel, C_0^\perp) = \sum_i^{\parallel,\perp} \sum_{k=1}^{N+1} \left| A^i e^{j\varphi^i(r, C_0^i, \lambda_k)} - A_m^i(\lambda_k) e^{j\delta_m^i(\lambda_k)} \right|$ across the design waveband] at each pixel coordinate (x, y) of the metadevice. Subsequently, the BAMMs can be constructed by choosing the optimal birefringent meta-atoms from the database for each (x, y) via the corresponding figure of merit with the selected $C_0^{\parallel,\perp}$. In the optimal program, we sampled many closely spaced frequency points in the broad bandwidth for approximating a continuous spectrum. Last, we adopt the PML boundary condition for all boundaries to carry out the 3D FDTD simulations for the metadevices.

SUPPLEMENTARY MATERIALS

Supplementary material for this article is available at http://advances.sciencemag.org/cgi/content/full/6/37/eabc0711/DC1

REFERENCES AND NOTES

1. A. C. Overvig, S. Shrestha, S. C. Malek, M. Lu, A. Stein, C. Zheng, N. Yu, Dielectric metasurfaces for complete and independent control of the optical amplitude and phase. *Light Sci. Appl.* **8**, 92 (2019).
2. N. Yu, P. Genevet, M. A. Kats, F. Aieta, J.-P. Tetienne, F. Capasso, Z. Gaburro, Light propagation with phase discontinuities: Generalized laws of reflection and refraction. *Science* **334**, 333–337 (2011).
3. J. P. B. Mueller, N. A. Rubin, R. C. Devlin, B. Groever, F. Capasso, Metasurface polarization optics: Independent phase control of arbitrary orthogonal states of polarization. *Phys. Rev. Lett.* **118**, 113901 (2017).
4. A. Arbabi, Y. Horie, M. Bagheri, A. Faraon, Dielectric metasurfaces for complete control of phase and polarization with subwavelength spatial resolution and high transmission. *Nat. Nanotechnol.* **10**, 937–943 (2015).
5. Z. Shi, M. Khorasaninejad, Y.-W. Huang, C. Roques-Carmes, A. Y. Zhu, W. T. Chen, V. Sanjeev, Z.-W. Ding, M. Tamagnone, K. Chaudhary, R. C. Devlin, C.-W. Qiu, F. Capasso, Single-layer metasurface with controllable multiwavelength function. *Nano Lett.* **18**, 2420–2427 (2018).
6. S. M. Kamali, E. Arbabi, A. Arbabi, Y. Horie, M. Faraji-Dana, A. Faraon, Angle-multiplexed metasurfaces: Encoding independent wavefronts in a single metasurface under different illumination angles. *Phys. Rev. X* **7**, 041056 (2017).
7. Y.-Y. Xie, P.-N. Ni, Q.-H. Wang, Q. Kan, G. Briere, P.-P. Chen, Z.-Z. Zhao, A. Delga, H.-R. Ren, H.-D. Chen, C. Xu, P. Genevet, Metasurface-integrated vertical cavity surface-emitting lasers for programmable directional lasing emissions. *Nat. Nanotechnol.* **15**, 125–130 (2020).
8. T.-Y. Huang, R. R. Grote, S. A. Mann, D. A. Hopper, A. L. Exarhos, G. G. Lopez, G. R. Kaighn, E. C. Garnett, L. C. Bassett, A monolithic immersion metalens for imaging solid-state quantum emitters. *Nat. Commun.* **10**, 2392 (2019).
9. C. Huang, C. Zhang, S. Xiao, Y. Wang, Y. Fan, Y. Liu, N. Zhang, G. Qu, H. Ji, J. Han, L. Ge, Y. Kivshar, Q. Song, Ultrafast control of vortex microlasers. *Science* **367**, 1018–1021 (2020).
10. G. Li, B. P. Clarke, J.-K. So, K. F. MacDonald, N. I. Zheludev, Holographic free-electron light source. *Nat. Commun.* **7**, 13705 (2016).
11. L. Jin, Z. Dong, S. Mei, Y. Yu, Z. Wei, Z. Pan, S. Rezaei, X. Li, A. I. Kuznetsov, Y. S. Kivshar, J. K. W. Yang, C.-W. Qiu, Noninterleaved Metasurface for $(2^6$-1$)$ Spin- and Wavelength-Encoded Holograms. *Nano Lett.* **18**, 8016–8024 (2018).
12. Y. Hu, L. Li, Y. Wang, M. Meng, L. Jin, X. Luo, Y. Chen, X. Li, S. Xiao, H. Wang, Y. Luo, C.-W. Qiu, H. Duan, Trichromatic and tripolarization-channel holography with noninterleaved dielectric metasurface. *Nano Lett.* **20**, 994–1002 (2020).
13. G. Zheng, H. Mühlenbernd, M. Kenney, G. Li, T. Zentgraf, S. Zhang, Metasurface holograms reaching 80% efficiency. *Nat. Nanotechnol.* **10**, 308–312 (2015).
14. X. Guo, Y. Ding, Y. Duan, X. Ni, Nonreciprocal metasurface with space–time phase modulation. *Light Sci. Appl.* **8**, 123 (2019).
15. M. Lawrence, J. A. Dionne, Nanoscale nonreciprocity via photon-spin-polarized stimulated Raman scattering. *Nat. Commun.* **10**, 3297 (2019).
16. S. Chen, Z. Li, H. Cheng, J. Tian, From single-dimensional to multidimensional manipulation of optical waves with metasurfaces. *Adv. Mater.* **31**, 1802458 (2019).
17. J. Jin, M. Pu, Y. Wang, X. Li, X. Ma, J. Luo, Z. Zhao, P. Gao, X. Luo, Multi-channel vortex beam generation by simultaneous amplitude and phase modulation with two-dimensional metamaterial. *Adv. Mater. Technol.* **2**, 1600201 (2016).
18. C. Chen, W. Song, J.-W. Chen, J.-H. Wang, Y. H. Chen, B. Xu, M.-K. Chen, H. Li, B. Fang, J. Chen, H. Y. Kuo, S. Wang, D. Tsai, S. Zhu, T. Li, Spectral tomographic imaging with aplanatic metalens. *Light Sci. Appl.* **8**, 99 (2019).
19. N. A. Rubin, G. Aversa, P. Chevalier, Z. Shi, W. T. Chen, F. Capasso, Matrix Fourier optics enables a compact full-Stokes polarization camera. *Science* **365**, eaax1839 (2019).
20. A. Y. Zhu, W. T. Chen, J. Sisler, K. M. A. Yousef, E. Lee, Y.-W. Huang, C.-W. Qiu, F. Capasso, Compact *aberration*-corrected spectrometers in the visible using dispersion-tailored metasurfaces. *Adv. Optical Mater.* **7**, 1801144 (2019).
21. S. Han, S. Kim, S. Kim, T. Low, V. W. Brar, M. S. Jang, Complete complex amplitude modulation with electronically tunable graphene plasmonic metamolecules. *ACS Nano* **14**, 1166–1175 (2020).
22. Q. Wei, B. Sain, Y. Wang, B. Reineke, X. Li, L. Huang, T. Zentgraf, Simultaneous spectral and spatial modulation for color printing and holography using all-dielectric metasurfaces. *Nano Lett.* **19**, 8964–8971 (2019).
23. P. C. Wu, J.-W. Chen, C.-W. Yin, Y.-C. Lai, T. L. Chung, C. Y. Liao, B. H. Chen, K.-W. Lee, C.-J. Chuang, C.-M. Wang, D. P. Tsai, Visible metasurfaces for on-chip polarimetry. *ACS Photonics* **5**, 2568–2573 (2018).
24. W. Liu, Z. Li, Z. Li, H. Cheng, C. Tang, J. Li, S. Chen, J. Tian, Energy-tailorable spin-selective multifunctional metasurfaces with full fourier components. *Adv. Mater.* **31**, 1901729 (2019).
25. Z. Yang, Z. Wang, Y. Wang, X. Feng, M. Zhao, Z. Wan, L. Zhu, J. Liu, Y. Huang, J. Xia, M. Wegener, Generalized Hartmann-Shack array of dielectric metalens sub-arrays for polarimetric beam profiling. *Nat. Commun.* **9**, 4607 (2018).

26. E. Wang, L. Shi, J. Niu, Y. Hua, H. Li, X. Zhu, C. Xie, T. Ye, Multichannel spatially nonhomogeneous focused vector vortex beams for quantum experiments. *Adv. Optical Mater.* **7**, 1801415 (2019).

27. X. Zang, H. Ding, Y. Intaravanne, L. Chen, Y. Peng, J. Xie, Q. Ke, A. V. Balakin, A. P. Shkurinov, X. Chen, Y. Zhu, S. Zhuang, A multi-foci metalens with polarization-rotated focal points. *Laser Photonics Rev.* **13**, 1900182 (2019).

28. S. Gao, C.-S. Park, C. Zhou, S.-S. Lee, D.-Y. Choi, Twofold polarization-selective all-dielectric trifoci metalens for linearly polarized visible light. *Adv. Optical Mater.* **7**, 1900883 (2019).

29. E. Arbabi, A. Arbabi, S. M. Kamali, Y. Horie, A. Faraon, Controlling the sign of chromatic dispersion in diffractive optics with dielectric metasurfaces. *Optica* **4**, 628–632 (2017).

30. M. Khorasaninejad, Z. Shi, A. Y. Zhu, W. T. Chen, V. Sanjeev, A. Zaidi, F. Capasso, Achromatic metalens over 60 nm bandwidth in the visible and metalens with reverse chromatic dispersion. *Nano Lett.* **17**, 1819–1824 (2017).

31. F. Aieta, M. A. Kats, P. Genevet, F. Capasso, Multiwavelength achromatic metasurfaces by dispersive phase compensation. *Science* **347**, 6228–1345 (2015).

32. S. Wang, P. C. Wu, V.-C. Su, Y.-C. Lai, C. H. Chu, J.-W. Chen, S.-H. Lu, J. Chen, B. Xu, C.-H. Kuan, T. Li, S. Zhu, D. P. Tsai, Broadband achromatic optical metasurface devices. *Nat. Commun.* **8**, 187 (2017).

33. W. T. Chen, A. Y. Zhu, V. Sanjeev, M. Khorasaninejad, Z. Shi, E. Lee, F. Capasso, A broadband achromatic metalens for focusing and imaging in the visible. *Nat. Nanotechnol.* **13**, 220–226 (2018).

34. S. Wang, P. C. Wu, V.-C. Su, Y.-C. Lai, M.-K. Chen, H. Y. Kuo, B. H. Chen, Y. H. Chen, T.-T. Huang, J.-H. Wang, R.-M. Lin, C.-H. Kuan, T. Li, Z. Wang, S. Zhu, D. P. Tsai, A broadband achromatic metalens in the visible. *Nat. Nanotechnol.* **13**, 227–232 (2018).

35. M.-K. Chen, C. H. Chu, R. J. Lin, J.-W. Chen, Y.-T. Huang, T.-T. Huang, H. Y. Kuo, D. P. Tsai, Optical meta-devices: Advances and applications. *Jpn. J. Appl. Phys.* **58**, SK0801 (2019).

36. H.-H. Hsiao, Y. H. Chen, R. J. Lin, P. C. Wu, S. Wang, B. H. Chen, D. P. Tsai, Integrated resonant unit of metasurfaces for broadband efficiency and phase manipulation. *Adv. Optical Mater.* **6**, 1800031 (2018).

37. S. Shrestha, A. C. Overvig, M. Lu, A. Stein, N. Yu, Broadband achromatic dielectric metalenses. *Light Sci. Appl.* **7**, 85 (2018).

38. S. Thiele, K. Arzenbacher, T. Gissib, H. Giessen, A. M. Herkommer, 3D-printed eagle eye: Compound microlens system for foveated imaging. *Sci. Adv.* **3**, e1602655 (2017).

39. M. Schmid, S. Thiele, A. Herkommer, H. Giessen, Three-dimensional direct laser written achromatic axicons and multi-component microlenses. *Opt. Lett.* **43**, 5837–5840 (2018).

40. D. Chandler-Horowitz, P. M. Amirtharaj, High-accuracy, midinfrared (450 cm^{-1} <= ω <= 4000 cm^{-1}) refractive index values of silicon. *J. Appl. Phys.* **97**, 123526 (2005).